International Journal of Concrete Structures and Materials

RESEARCH Open Access

Seismic Behavior of Steel Reinforced Ultra-High Strength Concrete Composite Frame: Experimental and Numerical Study

Jian-cheng Zhang[1,2*], Xue-guo Jiang[3], Zi-kang Jia[1,3], Mao-sen Cao[4] and Jin-qing Jia[5]

Abstract

The seismic behavior of steel reinforced ultra-high strength concrete (SRUHSC) composite frame was investigated through finite element analysis (FEA) modeling. A FEA model for the seismic analysis of the SRUHSC frame was first established and verified with test results. The numerical model was subsequently used to study the seismic performance of the SRUHSC frame, including the *P-Δ* skeleton curves, the stiffness degradation, the failure mode, the subsequence mechanisms of plastic hinges and the stress–strain distribution. Finally, a parametric study was carried out to investigate the effect of salient parameters on the behavior of the SRUHSC frame. It was found that with the increment of the concrete strength, yield strength of steel, and linear stiffness ratio of beam to column, the horizontal load-bearing capacity and the elastic stiffness of the structure were improved, but there was no significant effect on the ductility. With the increment of the volume stirrup ratio and structural steel ratio, the horizontal load-bearing capacity and the ductility of the structure were both improved. However, with the increment of the axial-load ratio, there was no obvious change in the elastic stiffness of the structure, but the horizontal load bearing capacity and the ductility of the structure decreased obviously. In addition, the accuracy of a concrete constitutive model in the different degrees of constraint for the SRUHSC frame proposed by the authors was verified with the FEA model.

Keywords Steel reinforced ultra-high strength concrete (SRUHSC), Finite element analysis (FEA), Seismic behavior, Parametric study

1 Introduction

In the last several decades, the steel reinforced ultra-high strength concrete (SRUHSC) members have been extensively used as main structural components in large-scale structures and infrastructures, such as high-rise and super high-rise buildings, bridges and subway stations (Aboukifa & Moustafa, 2021; Krahl et al., 2018; Shafieifar et al., 2017; Wakjira et al., 2024). It has been noted that damage or collapse of large-scale structures can be serious consequences under seismic load (He et al., 2020; Ma et al., 2024; Wei et al., 2021). So it is of great importance to design the steel reinforced ultra-high strength concrete (SRUHSC) structure with sufficient strength, stiffness, as well as energy dissipation capacity (Chellapandian et al., 2018; Xu et al., 2021; Yan et al., 2021). It has been summarized that encasing structural steel and high-strength

Journal information: ISSN 1976-0485 / eISSN 2234-1315.

*Correspondence:
Jian-cheng Zhang
zjc5108@just.edu.cn
[1] School of Naval Architecture and Civil Engineering, Jiangsu University of Science and Technology, Zhangjiagang, China
[2] Industrial Technology Research Institute of Zhangjiagang, Jiangsu University of Science and Technology, Suzhou, China
[3] School of Civil Engineering and Architecture, Jiangsu University of Science and Technology, Zhenjiang, China
[4] The College of Mechanics and Materials, Hohai University, Nanjing, China
[5] The State Key Laboratory of Coastal and Offshore Engineering, Dalian University of Technology, Dalian, China

stirrups into ultra-high-strength concrete columns can significantly increase the curvature ductility of sections and axial compression ductility (Hung & Yen, 2021; Hung et al., 2018; Naeimi & Moustafa, 2020; Zhu et al., 2020). Moreover, SRUHSC structure is commonly used in lower stories of high-rise or super high-rise buildings to reduce the dimensions of columns to increase available floor area (Kim et al., 2024; Yang et al., 2023). These are critical regions in high-rise buildings that are often subjected to inelastic response under severe seismic loading, which can significantly influences the seismic response of high-rise buildings (Zhang et al., 2019). There have been several groups of studies on the design and performance of SRUHSC structures (Liu & Jia, 2018; Yao et al., 2014; Zhu et al., 2014, 2016).

However, as reviewed above, previous studies were focused more on the seismic performance of the separated SRUHSC components. There is still a lack of systematic studies and design methods such on the whole SRUHSC structure system, which hinders their applications in engineering constructions. The authors have conducted seismic tests on a two-bay and three-story SRUHSC composite frame specimen under low reversed cyclic loading (Ma et al., 2018; Zhang & Jia, 2016; Zhang et al., 2019). Test results indicated that the SRUHSC frame possess excellent ductility and energy dissipation capacity. It should be noted that while a series of valuable observations and analysis has been made based on the test results, the parameters employed in the tests, including the size of the specimens, the material properties, and load parameters, were quite limited due to the constraints of the test apparatus. To further study the seismic behavior of SRUHSC frame, numerical modeling is employed to carry out a systematic parametric study on the SRUHSC frame in the present work. A finite element analysis (FEA) model is first established to simulate its response under seismic loading. The concrete constitutive model in the different degrees of constraint is specially discussed in the FEA model. The feasibility of the FEA model is verified against test results from the authors. The FEA model is subsequently used to analyze the seismic performance of the SRUHSC frame, including the *P-Δ* skeleton curves, the stiffness degradation, the failure mode, the subsequence mechanisms of plastic hinges and the stress–strain distribution. The numerical simulation results were compared with the experimental results to verify the accuracy of the proposed model. A parametric analysis is finally conducted to investigate the effects of salient parameters on the seismic performance of the SRUHSC frame, including axial compression ratio, concrete strength, volume hoop ratio of the frame column, steel content ratio of the frame column, the yield strength of the steel bone in the frame column and the linear stiffness ratio of the frame beam and column. The main aim of this study is to analysis the influence of salient parameters on the seismic behavior of SRUHSC frame, and also provides a reference for its reasonable seismic design methods.

2 Experimental Program

A two-bay and three-story one-fourth scale SRUHSC frame specimen was tested under simulated earthquake loading conditions. According to the seismic fortification intensity of 8 degrees (0.2 g), Class II site and design earthquake, the frame structure was divided into the first group design. The concrete strength grade of the frame column is C100 and the concrete strength grade of the beam is C40. The slenderness ratio l_0/b of frame column was 6.0, 5.0 and 5.0, respectively. l_n/h of the frame beam is 8.38. See Fig. 1 for the geometric size of the specimen and the configuration of reinforcement and steel bones in the member. See Fig. 2 for the steel skeleton of the finished frame joints. The test materials used in this test are the same as those in the reference (Zhang et al., 2019), and the concrete, reinforcement and steel bones of each label

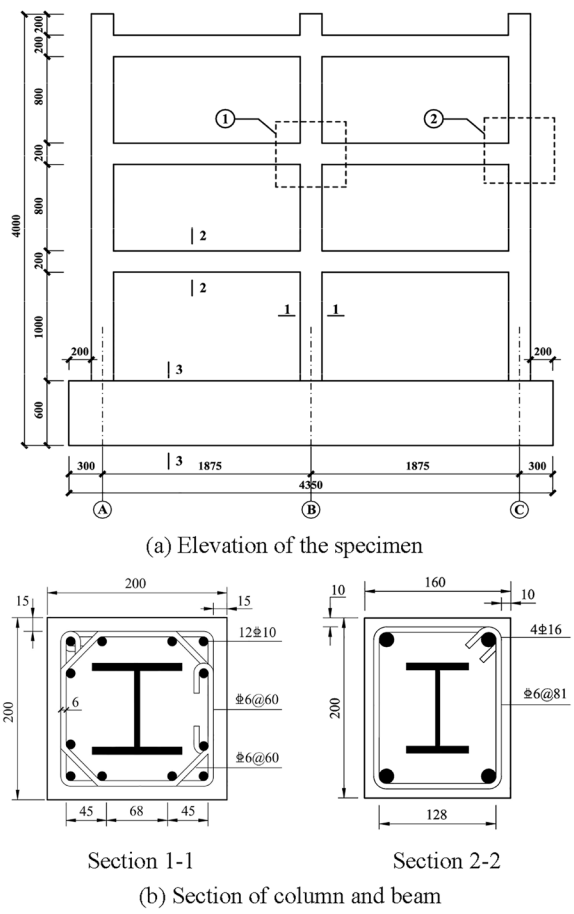

Fig. 1 Dimension and steel layout of specimen (unit: mm)

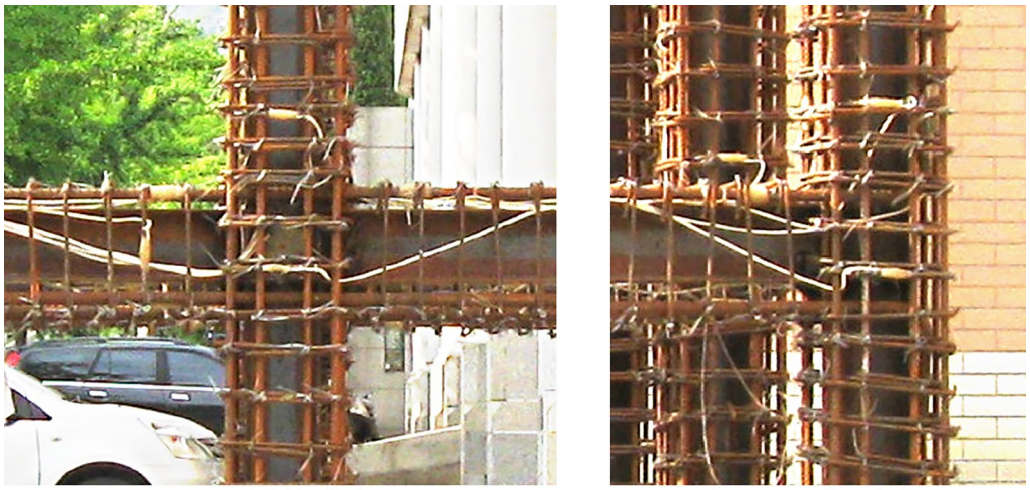

Fig. 2 Steel skeleton of frame joints

belong to the same batch as those in the reference (Zhang et al., 2019) and are poured together. In the test, the concrete composition content, steel and concrete measured mechanical indexes can be obtained by referring to the reference (Zhang et al., 2019). In the test, HRB400 ribbed rebar with a diameter of 10 mm and an average yielding strength of $f_y = 424$ MPa was used as longitudinal bars in columns. HRB400 ribbed rebar with a diameter of 6 mm and an average yielding strength of $f_y = 500$ MPa was used for transverse reinforcement. HRB335 ribbed rebar with a diameter of 16 mm and an average yielding strength of $f_y = 360$ MPa was used for longitudinal bars in beams. No. 10 I-shaped hot-rolled steel of Q235 with an average yielding strength of $f_y = 254$ MPa was adopted. In addition, the mean compressive strength f_{cm} of C100 concrete prisms reaches 105 MPa, the same as that of Specimen 1 in the reference (Zhang et al., 2019). In this paper, the axial pressure of middle column and side column is still set as 1600kN and 800kN, respectively. In addition, in the test, the arrangement of measuring instruments, installation of specimens, measuring contents and loading scheme of SRUHSC frame are all the same as those in reference (Zhang et al., 2019), and the horizontal loading mode of the top beam end is still adopted.

3 Test Results and Discussion

3.1 Hysteresis Curve and Failure Mode

The size of hysteresis curve can reflect the energy dissipation capacity of structure, which is the basis of the elastic–plastic analysis of seismic performance of structure. Fig. 3 is the hysteretic curve of the horizontal load P and its displacement Δ at the top beam end of the SRUHSC frame.

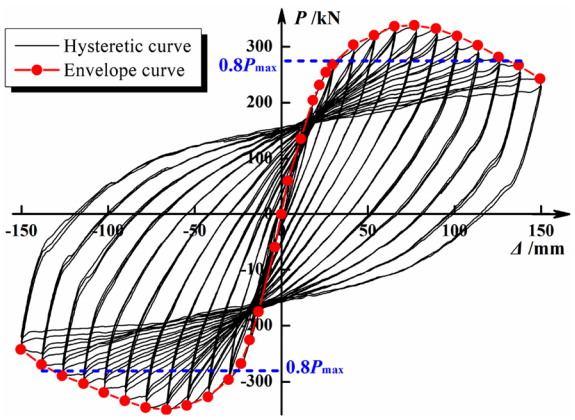

Fig. 3 Hysteretic curves of SRUHSC frame specimen

(1) At the initial stage of loading, the relationship between force and displacement is basically linear, and the changes in structural stiffness and residual deformation are small, indicating that the structure is still in the elastic working stage.
(2) As the loading displacement increases, cracks appear at the beam end of the frame specimen, and the hysteretic ring becomes fuller. The hysteretic track of force and displacement begins to bend, and the residual deformation begins to increase, indicating that the structure has entered the elasto-plastic working stage.
(3) The horizontal load increases with the increase of loading displacement until the structure yields, but the increase is small, indicating that the structure has good ductility and later bearing capacity. After

reaching the peak value, the horizontal load begins to decrease slowly and the structure enters the negative stiffness working stage. However, the area covered by the hysteresis ring of the structure is always increasing, indicating that the energy dissipation capacity of the frame structure is constantly increasing.

(4) Under low cyclic load, the shape of hysteretic curve of SRUHSC frame is basically symmetrical, round and full, indicating that the structure has good energy dissipation capacity and excellent seismic performance.

The final failure pattern of the SRUHSC frame structure is shown in Fig. 4.

3.2 Ductility and Interlayer Displacement Angle

The displacement ductility coefficient μ_Δ is usually used to reflect the deformation capacity of the structure, and its formula is $\mu_\Delta = \Delta_u/\Delta_y$, where Δ_u is the displacement at the time of failure and Δ_y is the displacement at the time of yield. Interlayer displacement angle $\theta_i = \Delta_i/h_i$, where Δ_i is the interlayer displacement during structural failure, and h_i is the height of each layer. The μ_Δ and θ of SRUHSC frame specimens are listed in Table 1.

Fig. 4 Failure mode of SRUHSC frame specimen

It can be seen from Table 1 that the μ_Δ of all parts of the frame are in the range of 4.32–6.06, indicating that the structure has good deformation ability and meets the design requirements of ductile frame (Zhang et al., 2019). In addition, GB5011-2010 requires that the elastic–plastic interlayer displacement angle (Δ_u/h) of reinforced concrete frame structure is 1/50, while the maximum elastic–plastic interlayer displacement angle of the structure in this paper is 1/20, which far exceeds the requirements of the code, indicating that the SRUHSC frame structure has good collapse resistance and plastic deformation ability, and excellent seismic performance.

3.3 Energy Dissipation

In this paper, the equivalent viscous damping coefficient h_e (Zhang et al., 2019) is used to reflect the energy dissipation capacity of the structure under repeated loads, which is listed in Table 2, where h_{ey}, h_{em} and h_{eu} are h_e of the structure under yield, ultimate load and failure, respectively. In addition, for comparison, h_e of steel-bone ordinary strength concrete frame structures at different working stages is also listed in the table (Zhang et al., 2019).

It can be seen from Table 2 that h_e of SRUHSC frame is larger than that of steel normal strength concrete frame in all stages of test loading, indicating that the structure has stronger energy dissipation capacity (Ma et al., 2018; Zhang & Jia, 2016).

4 Finite Element Analysis (FEA) Model

4.1 Material Constitutive Relationship

The object of analysis in this paper is the SRUHSC frame structure, that is, the composite frame of steel bone ultra-high strength concrete column and steel bone ordinary concrete beam. Due to the different constraints of concrete in different positions of members, the structure is divided into unrestrained concrete, medium restrained

Table 2 Equivalent viscous damping coefficients of specimen

h_e	h_{ey}	h_{em}	h_{eu}
Text specimens	0.092	0.145	0.295
Compare specimens	0.084	0.138	0.199

Table 1 Ductility coefficient and inter-story drift

Specimen	Global		1st story		2nd story		3rd story	
	+	−	+	−	+	−	+	−
μ_Δ	4.35	4.50	6.06	5.77	5.35	5.61	4.32	4.44
θ	1/24	1/24	1/22	1/23	1/21	1/21	1/29	1/30

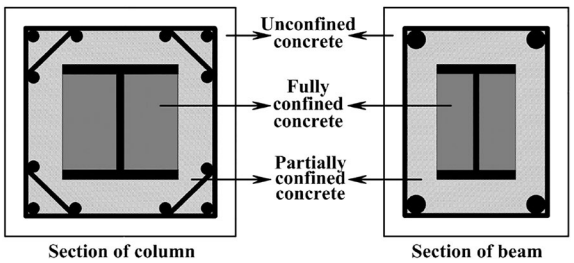

Fig. 5 Simplified sketch for confined concrete regions

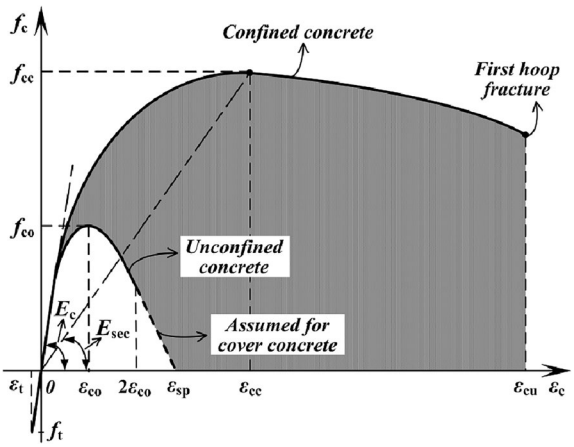

Fig. 6 Stress–strain model proposed for monotonic loading of confined and unconfined concrete

concrete and high restrained concrete. The concrete constraint area of its component section is divided, as shown in Fig. 5.

4.1.1 Constitutive Models for Constrained Concrete

In this paper, the test axial compressive strength (105 MPa) is adopted for the unconstrained ultra-high strength concrete, and the classical concrete constitutive model based on Mander model (Yang et al., 2023) is adopted for the constrained concrete, as shown in Fig. 6.

For quasi-static or monotone loading, the stress–strain relation of confined concrete is ascent stage,

$$f_c = \frac{f_{cc} x r}{r - 1 + x^r} \tag{1}$$

In the formula: f_{cc} is the axial compressive strength of restrained concrete.

$$x = \varepsilon_c / \varepsilon_{cc} \tag{2}$$

In the formula: ε_c is the longitudinal compressive strain of concrete, ε_{cc} is the strain corresponding to the peak stress of the confined concrete. For ε_{cc}, its expression is

$$\varepsilon_{cc} = \varepsilon_{co}\left[1 + 5\left(\frac{f_{cc}}{f_{co}} - 1\right)\right] \tag{3}$$

In the formula: f_{co} is the axial compressive strength of unrestrained concrete, ε_{co} is the strain corresponding to the peak stress f_{co} of unconstrained concrete, namely the peak compressive strain. For ordinary strength concrete, the ε_{co} is generally 0.002.

$$r = E_c/(E_c - E_{sec}) \tag{4.1}$$

$$E_{sec} = f_{cc}/\varepsilon_{co} \tag{4.2}$$

In the formula: $\boldsymbol{E_c}$ is the initial tangential modulus of concrete, $\boldsymbol{E_{sec}}$ is secant modulus of concrete, as shown in Fig. 6.

For ultra-high strength concrete ($\boldsymbol{f_{cu}}$>100 MPa), the equation below should be used to calculate the peak compressive strain $\boldsymbol{\varepsilon_{cc}}$ of confined concrete (Yang et al., 2023):

$$\varepsilon_{cc} = \varepsilon_{co}\left[1 + 5\left(\frac{55}{f_{co}}\right)\left(\frac{f_{cc}}{f_{co}} - 1\right)\right] \tag{5}$$

descent stage,

$$f_c = \frac{f_{cc} x r}{r - 1 + x^{d'r}} \tag{6.1}$$

$$d' = 1.0 + (d - 1)\sqrt{\frac{f_{cc} - f_c}{f_{cc}}} \tag{6.2}$$

residual stage,

$$f_c = 0.3 f_{cc} \tag{7}$$

For the compressive strength f_{cc} of the constrained concrete axis, the expression is

$$f_{cc} = f_{co}\left(-1.254 + 2.254\sqrt{1 + \frac{7.94 f_l'}{f_{co}}} - 2\frac{f_l'}{f_{co}}\right) \tag{8}$$

In the formula: f_{cc} and f_{co} are the compressive strength of concrete with and without constraints respectively, f_l' is the effective lateral confinement stress.

The effective lateral confinement stress f_l' in Eq. (8) is usually related to the configuration form of stirrup, stirrup spacing and effective confinement area of concrete, which is mathematically defined as

$$f_l' = f_l k_e \tag{9.1}$$

$$k_e = A_e/A_{cc} \tag{9.2}$$

In the formula: f_l is the lateral constraint stress of the stirrup (assuming that it is distributed on the surface

of the concrete core area), k_e is the effective constraint coefficient, A_e is the effective confined area of concrete, A_{cc} is the effective confined area of concrete surrounded by the central axis of the stirrup, and its mathematical expression is

$$A_{cc} = A_c(1 - \rho_{cc}) \tag{10}$$

In the formula: ρ_{cc} is the reinforcement rate of the longitudinal reinforcement in the section core area, that is, the ratio of the longitudinal reinforcement area to the section core area, A_c is the area of the core section of the concrete member.

The effective lateral confinement stress f_l' (Xiaowei et al., 2013) of concrete in medium and high confinement zones is described below.

(1) Concrete in medium confinement area f_l'

In reinforced concrete structure, the restraint of stirrup only acts on the core area. In Mander's model, it is assumed that there is a quadratic parabolic arch effect between adjacent longitudinal bars of concrete section, and the initial tangent angle is 45° (Yang et al., 2023). At this time, the effective restrained area of concrete should be the area of the concrete in the core area minus the sum of the axis lines between the longitudinal bars and the arch area enclosed by the assumed quadratic parabola. As the stirrups on concrete members are distributed discontinuously, the arch effect of the parabola exists between two adjacent stirrups in the longitudinal direction (i.e., section *Y–Y*) and between two adjacent longitudinal bars in the transverse direction (i.e., section *Z–Z*), as shown in Fig. 7.

The effective confined area A_e of concrete is

$$A_e = \left(b_c d_c - \sum_{i=1}^{n} A_i\right)\left(1 - \frac{s'}{2b_c}\right)\left(1 - \frac{s'}{2d_c}\right) \tag{11}$$

In the formula, s' is the longitudinal net distance of stirrup, b_c is the x-dimension of the concrete core area, d_c is the y-dimension of the concrete core area, A_i is the area surrounding the axis line between the ith longitudinal bars and the quadratic parabola, which is obtained by integration

$$A_i = \left(w_i'\right)^2/6 \tag{12}$$

In the formula, w_i' is the distance of the axis connection between the ith longitudinal ribs.

By further derivation, the effective constraint coefficient k_e is

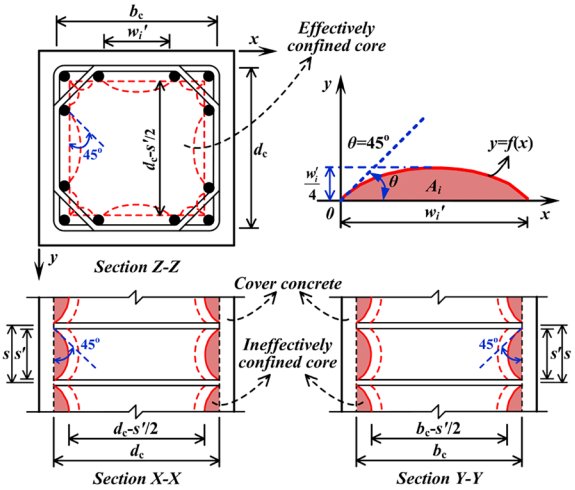

Fig. 7 Effectively confined core for multiple hoop reinforcement

$$k_e = \frac{A_e}{A_{cc}} = \frac{\left(1 - \sum_{i=1}^{n} \frac{(w_i')^2}{6b_c d_c}\right)\left(1 - \frac{s'}{2b_c}\right)\left(1 - \frac{s'}{2d_c}\right)}{(1 - \rho_{cc})} \tag{13}$$

The stirrup volume and stirrup ratio ρ_x and ρ_y in x and y directions of the section of steel-reinforced concrete member are, respectively,

$$\rho_x = A_{sx}/(sd_c) \tag{14.1}$$

$$\rho_y = A_{sy}/(sb_c) \tag{14.2}$$

In the formula: A_{sx} and A_{sy} are the total area of stirrups in the x and y directions, respectively, b_c is the x-dimension of the concrete core area, d_c is the y-dimension of the concrete core area, s is the space between stirrup configurations.

The lateral confinement stress f_{lx} and f_{ly} of stirrup in x and y directions are, respectively,

$$f_{lx} = \frac{A_{sx}}{sd_c} f_{yh} = \rho_x f_{yh} \tag{15.1}$$

$$f_{ly} = \frac{A_{sy}}{sb_c} f_{yh} = \rho_y f_{yh} \tag{15.2}$$

The effective lateral constraint stress f_{lx}' and f_{ly}' of stirrup in x direction and y direction are, respectively,

$$f_{lx}' = k_e \rho_x f_{yh} \tag{16.1}$$

$$f_{ly}' = k_e \rho_y f_{yh} \tag{16.2}$$

In the formula: k_e is the effective constraint coefficient, f_{yh} is the yield stress of stirrup.

(2) High restraint zone concrete f_l'.

Similar to the restraint of steel pipe on the concrete in its core area in the concrete filled steel tube structure, the derivation of the concrete enclosed f_l' by the section steel bone can be carried out. The constraining effect of square steel pipe on concrete in the core area is not uniformly distributed on the surface of the core area, but concentrated on the corner of the steel pipe. Based on the assumption of stirrup constraint on concrete in Mander model (Yang et al., 2023), the constraint effect of square steel pipe on concrete can also be assumed to be simplified into a quadratic parabolic arch effect between two adjacent corner points, whose initial cutting angle is still 45°. The schematic diagram of steel pipe constraint on concrete in the core area is shown in Fig. 8.

However, in the steel-reinforced concrete structure, the restraint effect of the built-in steel bone on the concrete in the core area is different from that of the ordinary rectangular concrete-filled steel tube (CFST), which is shown as follows (Xiaowei et al., 2013): (1) The external concrete can better prevent the local buckling and tearing of the section steel plate, (2) The steel bone is constrained by composite stirrup and concrete in the middle restraint zone, which indirectly strengthens the steel bone's constraint on the concrete in its core zone, (3) Compared with the closed steel pipe, the open steel bone weakens the constraint on the concrete in the core area. Therefore, the concrete in this area is the composite of the stirrup and its surrounding steel plate.

Similar to Eq. (12), in square concrete-filled steel tube, the arch area A_{ih} on one side of steel tube wall is

$$A_{ih} = b_{co}^2/6 \tag{17}$$

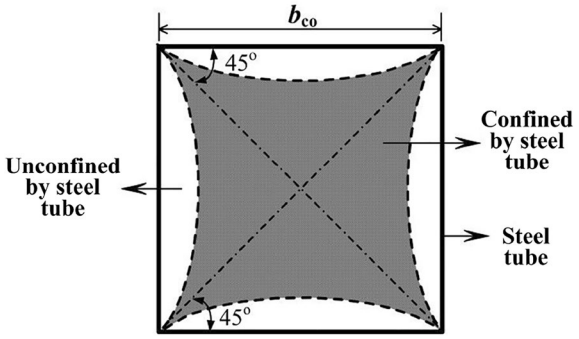

Fig. 8 Confinement effectiveness simplified sketch for concrete confined by steel tube

In the formula: b_{co} is the length of the side of the square steel pipe coated with concrete.

The area A_{cch} of steel pipe wrapped core concrete is

$$A_{cch} = b_{co}^2 \tag{18}$$

According to Eqs. (17) and (18), the effective constraint area $\boldsymbol{A_{eh}}$ of steel tube wrapped core concrete is

$$A_{eh} = A_{cch} - \sum_{i=1}^{n} A_{ih} = b_{co}^2 - 4 \cdot \frac{b_{co}^2}{6} = \frac{b_{co}^2}{3} \tag{19}$$

Then, according to Eqs. (9.2), (18) and (19), the effective constraint coefficient k_{eh} of concrete-filled steel tube is

$$k_{eh} = A_{eh}/A_{cch} = 1/3 \tag{20}$$

It is assumed that the constraints of steel pipe wall on concrete are uniformly distributed, in terms of the equilibrium of the forces

$$f_{lh} = f_y t_b / b_{co} \tag{21}$$

In the formula, f_{lh} is the lateral restraint stress of steel pipe on concrete, f_y is the yield stress of steel pipe, t_b is the sum of the thickness of the steel wall on both sides of the concrete-filled steel tube.

Therefore, the effective lateral confinement stress f_{lh}' of highly confined concrete is

$$f_{lh}' = f_{lh} k_{eh} = \frac{f_y t_b}{3 b_{co}} = \frac{f_y}{3 b_{co}} (t_w + t_f) \tag{22}$$

In the formula, f_{lh} is the lateral restraint stress of steel pipe on concrete, f_y is the yield stress of steel bones, t_w is the thickness of steel web, t_f is the thickness of steel flange, b_{co} is the length of the side of the section steel clad concrete.

In summary, the concrete stress–strain constitutive relationships of steel-reinforced concrete structures with three different constraints are shown in Fig. 9.

4.1.2 Constitutive Models for Steel Reinforcement and Steel Skeleton

Steel is modeled with the nonlinear combined isotropic and kinematic hardening model in ABAQUS (Abaqus Computer Software), which could well capture the Bauschinger effect under cyclic loading. To calibrate the parameters required for the kinematic hardening model, a stabilized cyclic for the steel material could be provided. Here in the cyclic stress–strain relationship recommended by Han and Yang (2023) is used to do the calibration. Results showed that the curve could predict the cyclic behavior of structural steel with good accuracy. For the isotropic hardening parameters, the measured values of the material parameters, such as elastic modulus E_s,

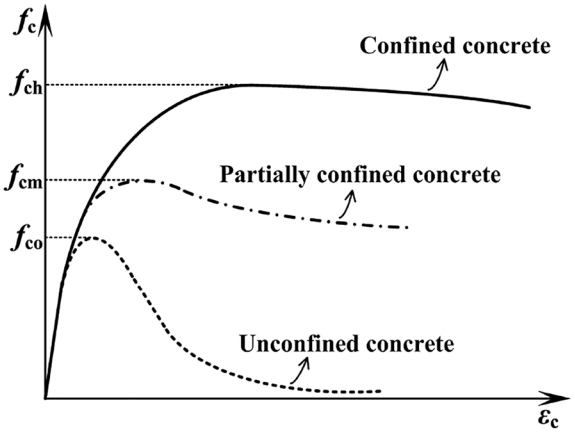

Fig. 9 Schematic diagram of constitutive model proposed for monotonic loading of confined and unconfined concrete

Poisson's ratio v, yield strength f_y, ultimate strength f_u and corresponding plastic strain ε, are employed (Yang et al., 2023).

4.2 Elements and Meshing

Eight-node space solid element is used for the modeling of the concrete components. Under the premise of the same grid division method, the results obtained using linear element or quadratic element in the model have little difference after calculation and comparison. Considering the computational efficiency of the model, linear element is more advantageous. Therefore, linear element is selected in this model, and the grid size of concrete element is set as 50 mm. Four-node space shell elements are used for the modeling of the steel bone, and the mesh size of steel bone element is also selected as 50 mm. Space truss element is used for both the reinforcements, and the mesh size of reinforcement unit is 200 mm.

4.3 Boundary Conditions and Loading Modes

The finite element simulation in this paper adopts the same boundary conditions and loading modes as the test:

(1) Boundary conditions: There are several interfaces in the FEA model between different components, e.g., the frame foundation is set as a fixed connection with the rigid ground, and the displacement and rotation in x, y and z directions are limited to ensure that the foundation will not move during the loading process. The fixed hinge constraints are set on the bottom of the foundation. Rotary hinge supports are set on the left and right sides of the foundation to limit the displacement in the x and z directions and ensure that the foundation of the frame structure will not have any sliding or rotation during the test.

(2) Loading modes: Based on the real test, two loading steps are required for the finite element model in this paper. The first step is to apply a constant axial load at the end of each column. The second step is to apply horizontal load on the top beam end of the frame. To ensure the convergence of the finite element calculation results, the loading mode of horizontal load is controlled by displacement. Test results indicated that when the horizontal displacement of the SRUHSC frame specimen reached 155 mm, the structure failed. Therefore, the boundary conditions are set to 155 mm in the FEA model.

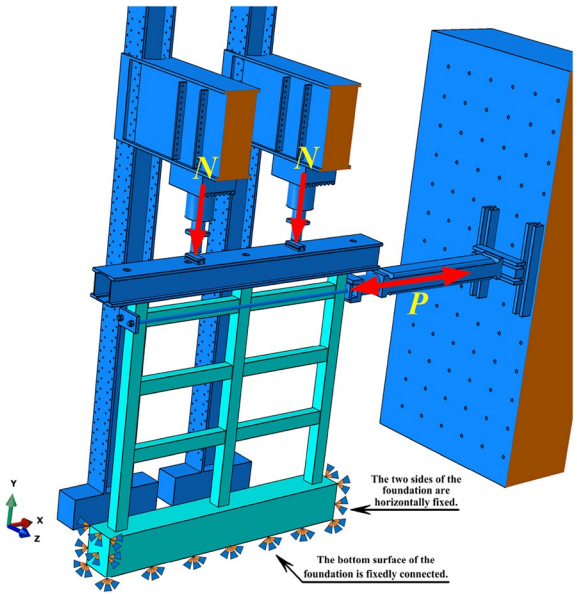

Fig. 10 Boundary conditions and loads of frame model

The boundary conditions and loading modes of the model are shown in Fig. 10.

4.4 Defining Interactions

In the test, the bond slip between steel bone and concrete will have a certain influence on the structural force, but according to relevant data (Barbero, 2023), for ultra-high strength concrete structures, the results obtained by considering bond slip are more accurate, but it has little effect on the calculation accuracy if neglected, and it can still meet the engineering requirements. On the contrary, the computational efficiency of the model is greatly improved. Therefore, the contact relationships between steel bone and concrete and steel bar and concrete are defined by Embedded method (Barbero, 2023).

According to the above methods, the finite element model of SRUHSC frame structure was established, as shown in Fig. 11.

4.5 Verifications of the FEA Model

With two major features of the FEA model verified against test data, the complete FEA model is then verified against the test results on the skeleton curve and stiffness curve for SRUHSC frame. The skeleton curve and stiffness curve calculated by FEA are compared with the measured results in the test, as shown in Fig. 12. The structure is set as the yield point when the first plastic hinge at the beam end is generated, the peak point when the horizontal load reaches its maximum value, and the end point when the loading ends. Table 3 lists the calculated and measured values of the above three characteristic loads and their corresponding displacements, and makes a comparative analysis.

It can be seen from Fig. 12 and Table 3 that:

In the elastic stiffness of the structure, the calculated value of the numerical simulation is slightly larger than the measured value. With the continuous loading, the calculated value of structural stiffness decreases faster and reaches the peak point earlier than the measured value, so that the corresponding peak displacement is smaller than the measured value. The ratio between the numerical simulation and the measured peak load is 1.01, and the difference is only 0.76%. When the structure enters the negative stiffness stage, the closeness between the *P-Δ* curve calculated by numerical simulation and the skeleton curve measured by experiment gradually becomes worse, and the separation trend between them becomes more and more obvious. However, it can be

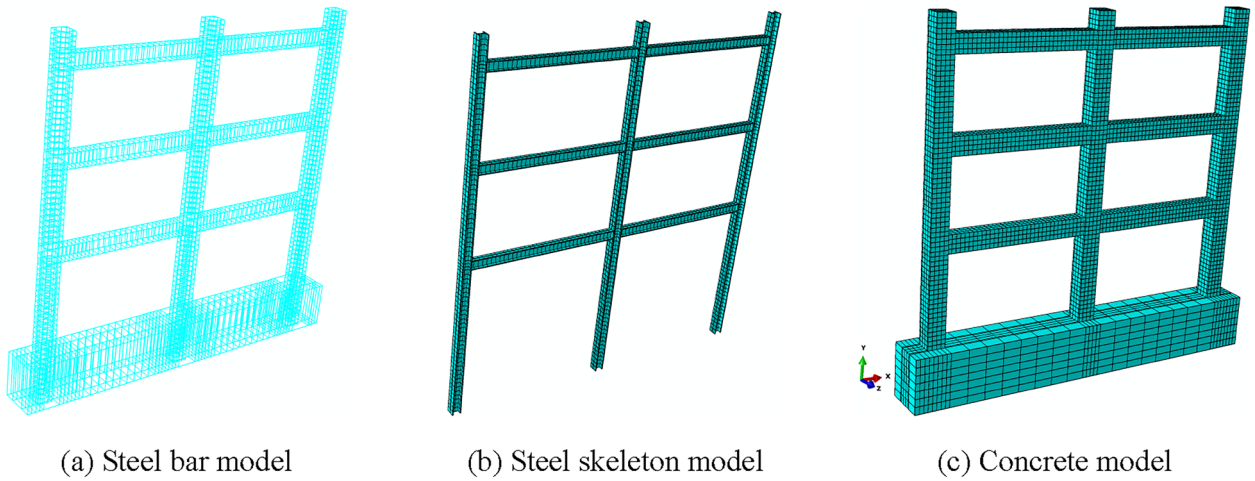

Fig. 11 Schematic view of FEA model

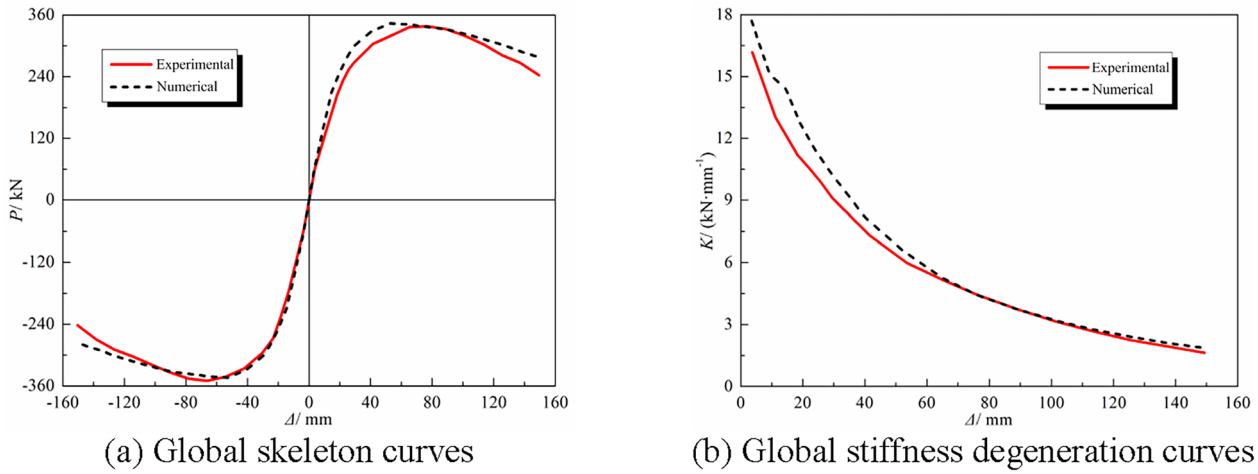

Fig. 12 Comparison between experimental and numerical calculated results of frame

Table 3 Comparison between calculated and experimental result of SRUHSC frame under different load conditions

loading stage	P_c/kN	Δ_c/mm	P_e/kN	Δ_e/mm	P_c/P_e	Δ_c/Δ_e
Cracking	274.3	24.8	282.8	30.4	0.97	0.82
Maximum load	343.7	59.4	341.1	65.9	1.01	0.91
Ultimate failure	275.1	155.0	243.2	155.0	1.13	1.00

P_c and Δ_c are the calculated values of the loads and displacements in the numerical simulation of the SRUHSC frame for each loading phase, respectively. Moreover, P_e and Δ_e are the measured values of the loads and displacements in the Quasi-static test of the SRUHSC frame for each loading phase, respectively

seen from Fig. 12b that they tend to be consistent and closer in terms of structural stiffness. In general, the overall skeleton curve and stiffness degradation curve of the structure, the calculated values of the numerical simulation are in good agreement with the measured values in the test, which verifies the correctness and effectiveness of the finite element model established in this paper.

The reasons for the deviation between the calculated value and the measured value are as follows:

(1) In the test, the real loading mode is cyclic loading. To ensure its convergence, the monotone loading mode is adopted in the calculation. As a result, the calculated damage degree of the model structure is less serious than the actual situation, and the structural stiffness decline slows down.
(2) In the test, due to the need to apply horizontal reciprocating load to the specimen, the horizontal force transfer screw is installed on the top layer of the frame. Although high-strength bolts are tightened before loading, the structural damage is gradually aggravated as the loading goes on and the concrete at the beam end and column end keeps cracking and spalling, and the originally tightened bolts become loose, resulting in deformation. As a result, the measured displacement of the beam end of the top layer of the frame is larger than the calculated value. In addition, the measured value of structural stiffness is smaller than the calculated value to some extent.
(3) The finite element model in this paper does not consider the bond slip between steel bone and concrete. However, in the actual loading process, especially in the late loading period, the structure enters the negative stiffness stage, and a certain degree of slip between steel bone and concrete is inevitable, which leads to the calculated value of structural stiffness in the initial loading period being larger than the measured value.

Fig. 13 shows the comparison between the numerical simulation values and the measured values of the horizontal load P-interlayer displacement Δ_i ($i=1, 2, 3$) skeleton curves and the stiffness between each layer. As can be seen from the figure, the curves of both sides have a good coincidence, and the law presented is similar to the calculation results of the overall frame structure, indicating that the deformation results of each layer of the frame structure calculated by finite element are consistent with the actual conditions in the test, which further verifies the validity and correctness of the finite element model established in this paper from the side.

4.6 Analysis of Plastic Hinge Sequence

In the test, the different location and sequence of plastic hinge will lead to different failure modes of the frame structure. For the position and sequence of plastic hinge generation in the frame model, the comparison between the results of finite element simulation and the results measured in the test is shown in Fig. 14. As shown in Fig. 14:

(1) It can be seen from the simulation results and measured results that the frame structure of this test is a "strong column and weak beam" type structure. Plastic hinges first occur at the left or right beam ends of the column in the first layer, and then at the beam ends of each layer of the frame. Plastic hinges only occur at the top of the column in the third layer and at the root of the bottom column after plastic hinges are produced at all beam ends.
(2) The exit hinge sequence between the calculated results and the measured results is different. The main reasons for this result are: (1) The measured mechanical properties of the steel used in the frame are different from the mechanical properties of its own type, and the material of the steel itself is not absolutely uniform. However, in the finite element model, the concrete and steel properties of the end of the frame beam are uniformly endowed, and all materials are evenly distributed. The frame beam has the same strength and bearing capacity, so that the hinge sequence is relatively regular. (2) Because the beam and column of the frame are made of concrete with different strengths, it is difficult to ensure that the two sides are distinct and do not interfere with each other when the actual beam and column joints are poured, which causes the concrete

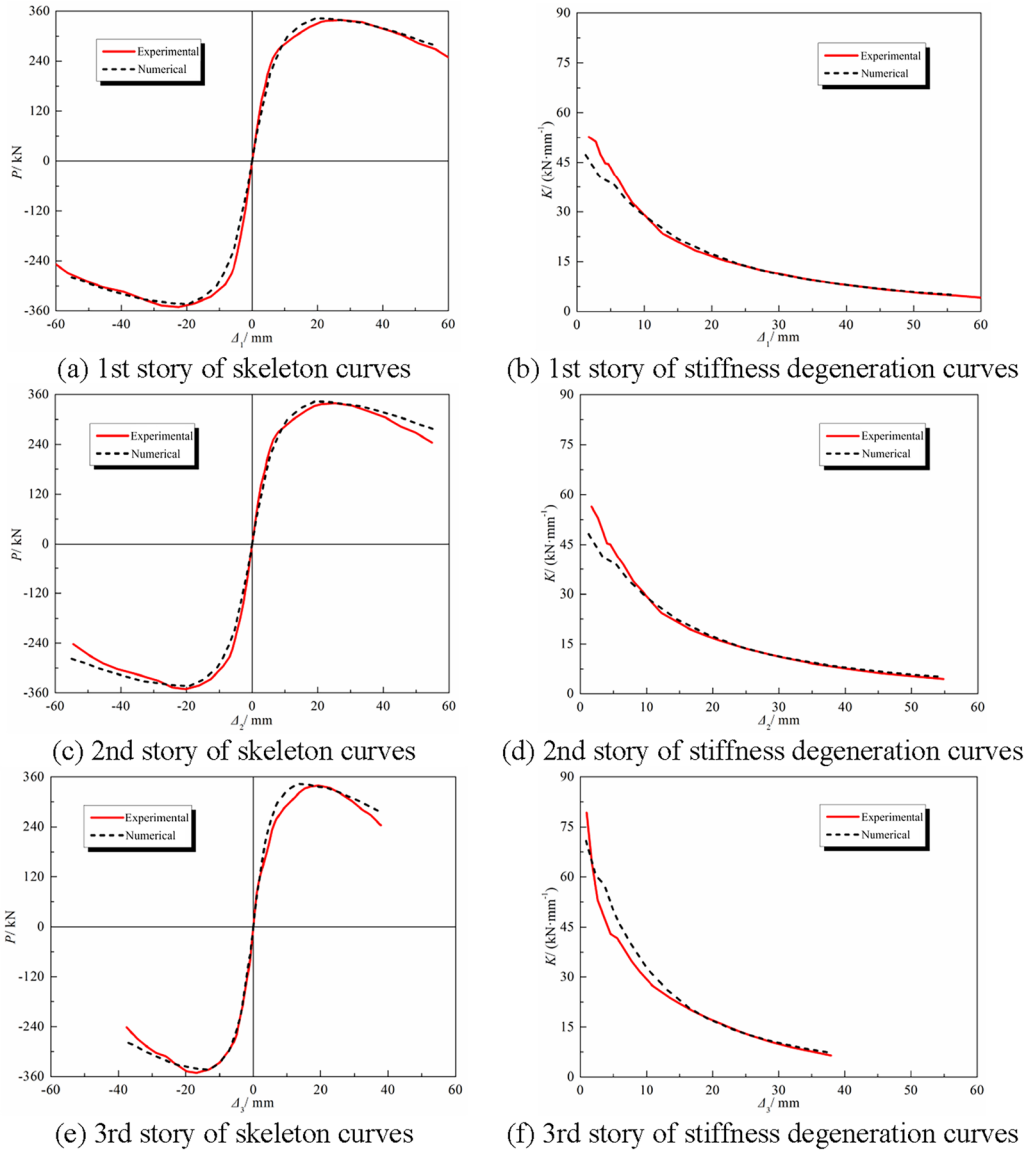

Fig. 13 Comparison between numerical calculated and experimental results of inter-stories

strength of each beam end in the actual structure to be slightly different, and the distribution law of the material strength becomes worse, resulting in the actual strength and bending bearing capacity of each beam end of the frame model to be different.

4.7 Stress–strain Distribution

Fig. 15 shows the stress–strain diagram of the frame when the horizontal load reaches its peak and the frame generates the maximum lateral displacement. It can be seen from the figure that the internal force distribution law and failure characteristics obtained by finite element simulation are basically the same as the test phenomenon, indicating that the finite element model established in this paper can reflect the actual situation of the test. When the frame reaches yield, the stress levels of the longitudinal reinforcement, the beam column and the stirrup in the core area of the joint are all in a low state, far less than their respective yield strength, indicating that the longitudinal reinforcement and stirrup in these parts are still in an elastic state. However, the maximum stress of the longitudinal bar at the end of the beam exceeds its yield strength. The maximum stress of the section steel of the frame specimen occurs near the beam-column junction, and the flange of the section steel does not reach the yield state, indicating that the bending

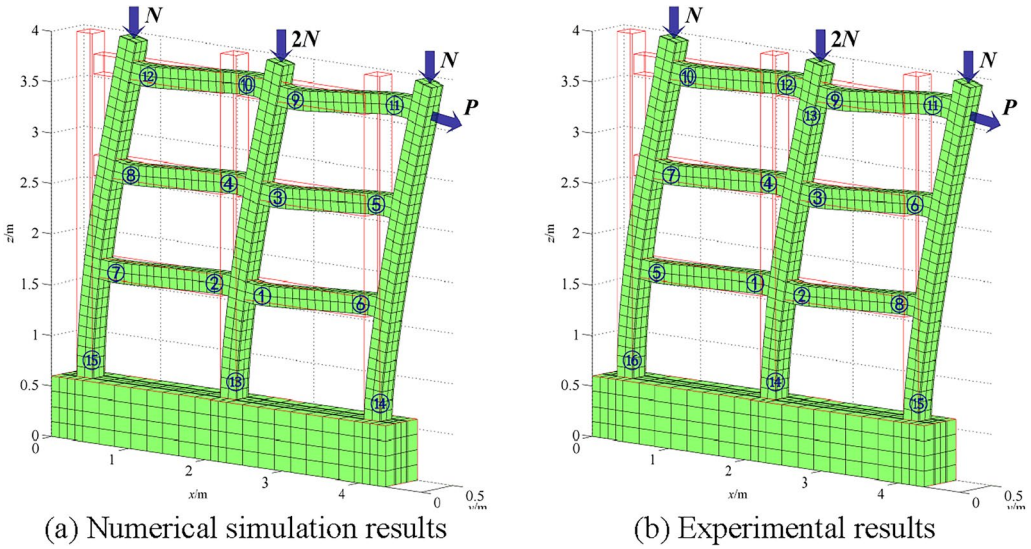

Fig. 14 Comparison between numerical and experimental results of plastic hinge development

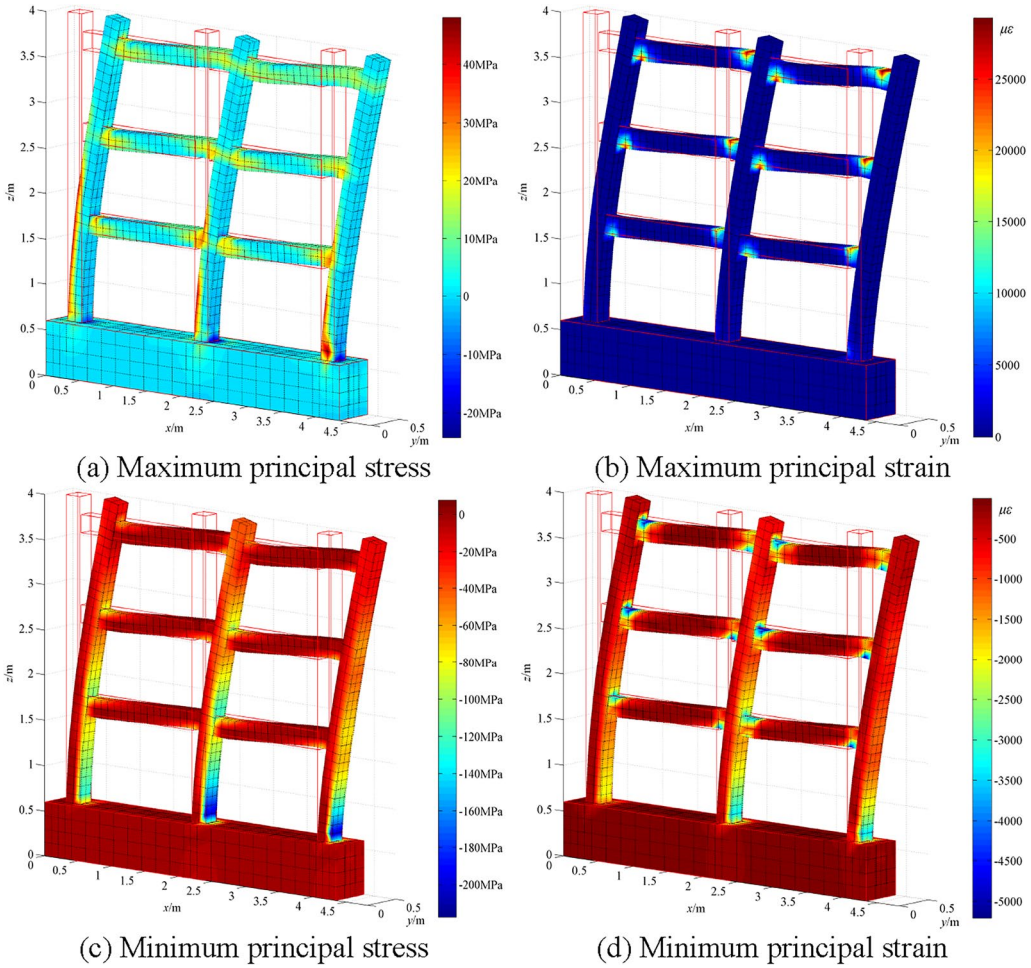

Fig. 15 Stress–strain contours of frame under max carrying capacity

failure of the plastic hinge area of the beam end occurs in the frame, which is consistent with the experimental phenomenon. The maximum stress and strain of concrete occur at the root of the bottom column and at the beam end of each layer, that is, the area where the cracks of the frame mainly develop and destroy, which is also consistent with the test results.

As reviewed above, the numerical simulation results are in good agreement with the experimental results, which indicates the correctness of the finite element model established in this paper, and also lays a foundation for the subsequent parameter analysis.

5 Parametric Study

Based on the established finite element model, to further study the SRUHSC frame structure and understand the influence of the main design parameters on the seismic performance of the structure, Six parameters, including axial compression ratio n, concrete strength f_{cu}, volumetric stirrup ratio of frame columns ρ_{sv}, the steel ratio of frame columns ρ_{ss}, the yield strength of structural steel in frame columns f_y and the beam-column's linear stiffness ratio of frame β, were selected for finite element analysis. To ensure its accuracy, when studying a parameter, other parameters remain unchanged.

5.1 Parameters of the Axial Compression Ratio *N*

With other parameters unchanged, the influence of axial compression ratio n on the mechanical properties of SRUHSC frame was studied only by changing the axial compression ratio n of the frame model column. The test axial compression ratio n was set as 0.0, 0.1, 0.2, 0.3, 0.4 and 0.5, respectively, and the design axial compression ratio was set as 0.0, 0.2, 0.4, 0.6, 0.8 and 1.0, respectively. It should be noted that the axial compression ratio here is the axial compression ratio of the column in the frame, and the axial compression ratio of the corresponding side column is taken as half of the middle column. The P-Δ skeleton curves of finite element simulation are shown in Fig. 16. Meanwhile, Table 4 shows the influence of axial compression ratio changes on the bearing capacity and deformation capacity of the frame at each loading stage.

As shown in Fig. 16 and Table 4,

(1) The axial compression ratio n has little influence on the elastic stiffness of the frame structure at the early loading stage, but has a great influence on the peak load of the frame and the negative stiffness segment that the structure enters later.
(2) When the axial compression ratio n is 0 (that is, no axial force action), the horizontal load of the model structure is 312.7kN when the plastic hinge at the first beam end is generated. When the load reaches its peak, the size is 388.9kN. After that, the horizontal bearing capacity of the structure declines gently compared with the peak value until the end of loading. The horizontal load of structural failure also decreased by only 3.16%.
(3) Due to the large height of the frame model, large lateral displacement will be generated under horizontal load, so the P-Δ effect is obvious. With the increase of axial compression ratio, the peak value of horizontal load also decreases. Compared with the peak value of load when axial compression ratio n is 0, the peak value of load when axial compression ratio are 0.1, 0.2, 0.3, 0.4 and 0.5 decreases by 1.90%, 3.52%, 7.20%, 12.2% and 17.1%, respectively. With the decrease of peak load P_m, The corresponding horizontal displacement Δ_m is also decreasing, and the specific influence situation is shown in Fig. 17.
(4) It can be seen from Fig. 17 that, with the increase of axial compression ratio, the structure declines more significantly at the negative stiffness stage (when the axial compression ratio increases from 0.1 to 0.5, the load P_e at the end point of loading decreases by 5.19%, 8.66%, 12.4%, 20.0% and 28.3%, respectively, compared with the peak load P_m of the structure). The displacement ductility of the frame decreases with the increase of the decreasing range.

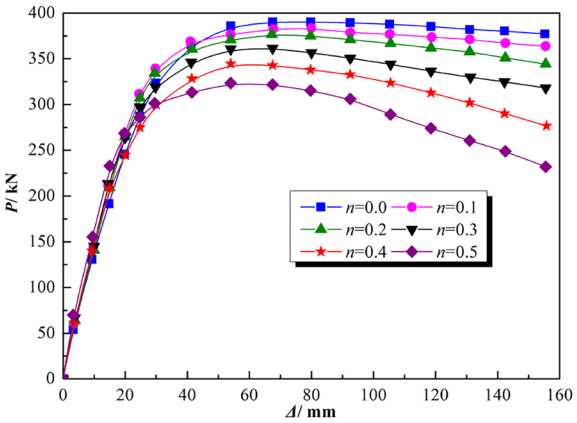

Fig. 16 The relationship of P-Δ of SRUHSC frame during the different axial-load ratios

5.2 Parameters of the Concrete Strength f_{cu}

With other parameters unchanged, the influence of concrete strength f_{cu} in the frame model column on the mechanical properties of SRUHSC frame was studied. Since the research object of this paper is the mechanical performance of steel-bone ultra-high strength concrete frame structure, the strength grade of concrete in the

Table 4 Influence of compression ratio on load bearing capacity and deformation under different load conditions

n	P_q/kN	P_m/kN	P_e/kN	Δ_q/mm	Δ_m/mm	Δ_e/mm
0.0	312.7	388.9	376.6	29.7	86.0	155.0
0.1	318.9	381.5	361.7	24.9	75.8	155.0
0.2	307.9	375.2	342.7	24.9	67.1	155.0
0.3	297.3	360.9	316.2	24.9	60.7	155.0
0.4	278.4	341.3	275.0	24.9	54.0	155.0
0.5	285.7	322.5	231.3	24.8	49.5	155.0

P_q is the calculated value of the horizontal load when the first beam end plastic hinge appears in the numerical simulation frame. P_m is the calculated peak value of the horizontal load of the numerical simulation frame. P_e is the calculated value of the horizontal load of the frame at the end of the numerical simulation load. Moreover, Δ_q, Δ_m and Δ_e are correspond to the calculated horizontal displacement values of P_q, P_m and P_e frame top beam ends, respectively

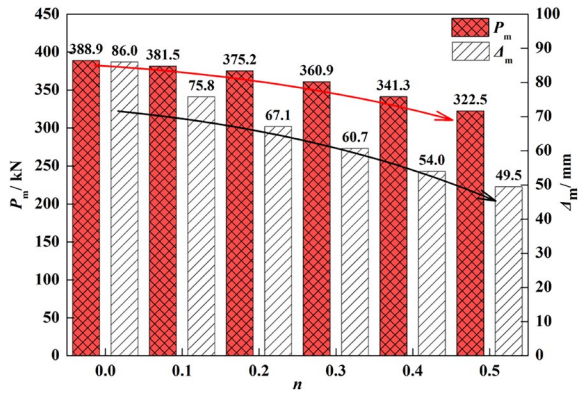

Fig. 17 Influence of peak load and corresponding deflection of SRUHSC frame during the different axial-load ratios

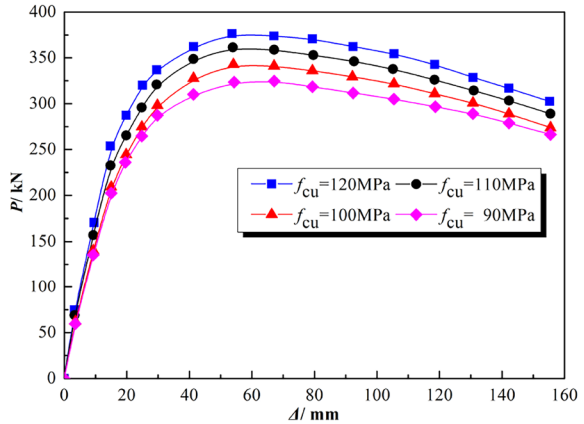

Fig. 18 The relationship of *P*-*Δ* curves of SRUHSC frame during the different concrete strengths

column must be high strength or above, so the strength grade of concrete is 90 MPa, 100 MPa, 110 MPa and 120 MPa respectively. The *P*-*Δ* skeleton curves of finite element numerical simulation are shown in Fig. 18. Meanwhile, Table 5 shows the influence of concrete strength change on the bearing capacity and deformation capacity of the structure at each loading stage. The symbols in Table 5 have the same meaning as Table 4.

As shown in Fig. 18 and Table 5,

(1) When the f_{cu} is 90 MPa, the horizontal load of the model structure when the plastic hinge at the first beam end is 256.7 kN, when the load reaches its peak, the size is 324.3 kN, and when the load reaches the end of loading, the load value at the end point is 267.6 kN, which decreases by 17.5%.

(2) The change of concrete strength has a certain effect on the initial stiffness of the structure and the peak of the horizontal bearing capacity. The bearing capacity of the normal section of the frame column increases with the increase of the strength of concrete, and the higher the strength of concrete, the stronger the wrapping capacity of the internal steel bone, and the initial stiffness and peak load of the elastic section of the structure also increase. Compared with the peak load of the structure whose concrete strength are 90 MPa, when f_{cu} are 100 MPa, 110 MPa and 120 MPa, the peak load of the structure increases by 5.98%, 11.6% and 16.2%, respectively. The horizontal displacement Δ_m of the top beam end corresponding to the peak load P_m of the frame structure also decreases continuously. See Fig. 19.

(3) As the concrete strength increases from 90 to 120 MPa, the load P_e at the end point of the structure at the end of loading decreases by 17.5%, 20.0%, 19.8% and 19.7%, respectively, compared with the peak load P_m. The negative stiffness segments of each skeleton curve have a large decline, and the decline amplitude of the negative stiffness segments of the last three strength levels is similar, indicating that when the concrete strength enters the category of ultra-high strength ($f_{cu} \geq 100$ MPa), simply

Table 5 Influence of concrete strength on load bearing capacity and deformation under different load conditions

f_{cu}/MPa	P_q/kN	P_m/kN	P_e/kN	Δ_q/mm	Δ_m/mm	Δ_e/mm
90	256.7	324.3	267.6	23.4	64.2	155.0
100	274.3	343.7	275.1	24.8	59.4	155.0
110	295.5	361.8	290.2	24.8	57.8	155.0
120	319.6	376.9	302.6	24.8	53.2	155.0

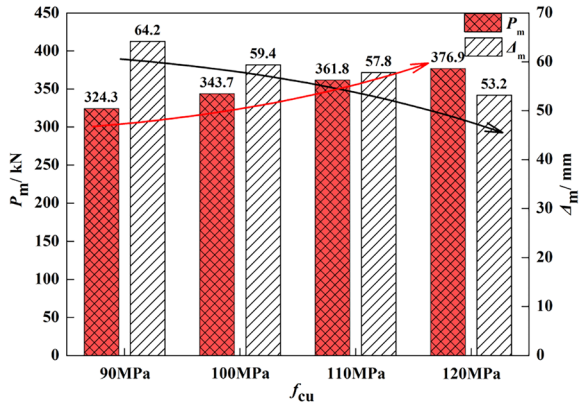

Fig. 19 Influence of peak load and corresponding deflection of SRUHSC frame during the different concrete strengths

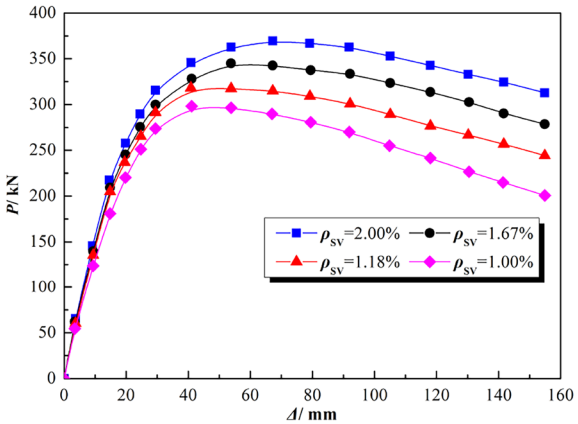

Fig. 20 The relationship of *P*-*Δ* of SRUHSC frame during the different volume stirrup ratios

improving the concrete strength has little effect on the ductility of the structure.

5.3 Parameters of the Volumetric Stirrup Ratio of Frame Columns P_{sv}

With other parameters unchanged, the effect of ρ_{sv}, the volumetric stirrup ratio of the frame column, on the mechanical properties of SRUHSC frame was studied. The density of stirrup layout is directly related to whether the concrete can be effectively restrained, thus affecting the mechanical performance of the whole structure. The frame column of this model uses eight deformation composite stirrup, and the volume stirrup ratio ρ_{sv} of the column can be changed by configuring different intervals of stirrup. The stirrup spacing was set as 50 mm, 60 mm, 85 mm and 100 mm, and the corresponding volume stirrup ρ_{sv} was 2.00%, 1.67%, 1.18% and 1.00%, respectively. The *P*-*Δ* skeleton curves of finite element simulation are shown in Fig. 20. At the same time, Table 6 shows the influence of the change of the volume ferrule ratio on the bearing capacity and deformation capacity of the structure at each loading stage. The meanings of symbols in Table 6 are the same as those in Table 4.

As shown in Fig. 20 and Table 6:

(1) With the decrease of stirrup spacing and the increase of volume stirrup ratio, the restraint effect on concrete is gradually strengthened, and the initial stiffness and peak load of the structure also increase.

(2) When ρ_{sv} is 1.00% (i.e., the distance between the hooped joints is 100 mm), the horizontal load of the model structure when producing the first beam end plastic hinge is 204.8 kN, when the load reaches the peak, the size is 296.3 kN, and until the end of the loading, the load value of the end point is 199.6 kN, decreased by 32.6%.

(3) Compared with the structural peak load ρ_{sv} of 1.00%, when ρ_{sv} is 1.18%, 1.67% and 2.00%, the peak load of the structure increases by 6.92%, 16.0% and 24.4%, respectively. The horizontal displacement Δ_m of the top beam end corresponding to the peak load P_m of the structure also increases continuously (see Fig. 21). It indicates that the energy dissipation capacity of the structure is increasing continuously.

(4) ρ_{sv} of volume stirrup ratio increased from 1.00% to 2.00%, and the load P_e at the end point decreased by 32.8%, 23.1%, 19.9% and 15.2% compared with their peak load P_m, respectively. The decreasing range indicated that the downward trend of negative stiffness section of each skeleton curve was gradually gentle, and the structure ductility was continuously strengthened.

Table 6 Influence of volume stirrup ratio on load bearing capacity and deformation under different load conditions

ρ_{sv} (%)	P_q/kN	P_m/kN	P_e/kN	Δ_q/mm	Δ_m/mm	Δ_e/mm
1.00	204.8	296.3	196.8	18.2	39.6	155.0
1.18	237.6	316.8	243.7	20.4	41.3	155.0
1.67	274.3	343.7	275.1	24.8	59.4	155.0
2.00	310.8	368.5	312.5	28.6	67.4	155.0

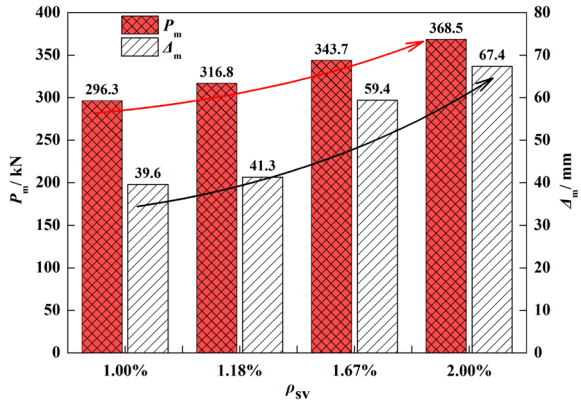

Fig. 21 Influence of peak load and corresponding deflection of SRUHSC frame during the different volume stirrup ratios

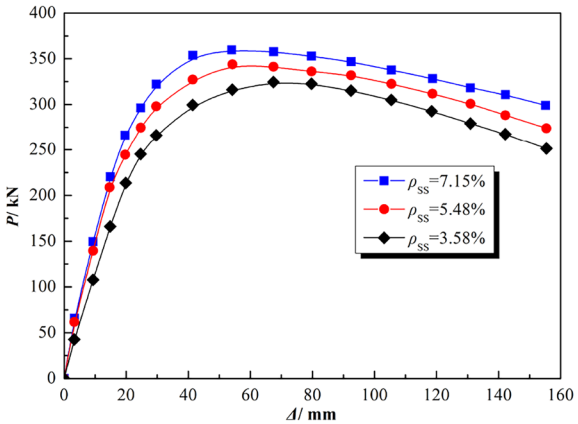

Fig. 22 The relationship of *P-Δ* of SRUHSC frame during the different structural steel ratios

5.4 Parameters of the Steel Ratio of Frame Columns P_{ss}

With other parameters unchanged, the effect of ρ_{ss} on the seismic performance of SRUHSC frame was studied by changing the steel content in the frame column. The steel bones of the frame column are I-section steel, H-section steel and cross section steel, among which I-section steel is I10, H-shaped steel HW10, The cross section steel is welded from two I10 sections. The ρ_{ss} was 3.58%, 5.48% and 7.15%, respectively. The *P-Δ* skeleton curves of finite element simulation are shown in Fig. 22. At the same time, Table 7 shows the influence of steel content change on the bearing capacity and deformation capacity of the structure at each loading stage. The meanings of symbols in Table 7 are the same as those in Table 4.

As shown in Fig. 22 and Table 7:

(1) With the increase of steel content in the column, the stiffness and horizontal bearing capacity of the frame model in the elastic–plastic stage are increased, and the decreasing range of the decreasing stage is also slightly decreased. However, the steel content mainly affects the value of the curve, and has little influence on the overall shape and trend of the *P-Δ* skeleton curve.

(2) When the ρ_{ss} is 3.58% (that is, the column steel bone configuration I10 type steel), the horizontal load of the model structure in the generation of the first beam end plastic hinge is 225.7kN, when the load reaches the peak, the size is 324.8kN, and until the end of the loading, the load value of the end point is 252.3kN, the peak load decreased by 22.3%.

(3) Compared with the structural peak ρ_{ss} of 3.58%, p_{ss} was 5.48% and 7.15% (i.e., the column with H-beam and cross beam), and the peak value of the horizontal load increased by 5.82% and 11.0%, respectively, and the horizontal displacement Δ_m of the top beam end corresponding to the peak load P_m decreased continuously, as shown in Fig. 23.

(4) With the increase of steel content, the higher constraint area of column section becomes larger and its binding force on the concrete in the core area is strengthened. The load P_e at the end point of the structure decreases by 22.3%, 19.9% and 16.8%, respectively, compared with the peak load P_m of the structure. The decreasing range shows the increased ductility of the structure.

5.5 Parameters of the Yield Strength of Structural Steel in Frame Columns F_y

With other parameters unchanged, the influence of the yield strength f_y of the steel bone in the frame model column on the mechanical properties of SRUHSC frame was studied. Grade Q235, Q345, Q390 and Q420 steels are

Table 7 Influence of structural steel ratio on load bearing capacity and deformation under different load conditions

ρ_{ss} (%)	P_q/kN	P_m/kN	P_e/kN	Δ_q/mm	Δ_m/mm	Δ_e/mm
3.58	225.7	324.8	252.3	21.7	67.4	155.0
5.48	274.3	343.7	275.1	24.8	59.4	155.0
7.15	315.4	360.5	300.2	28.3	56.0	155.0

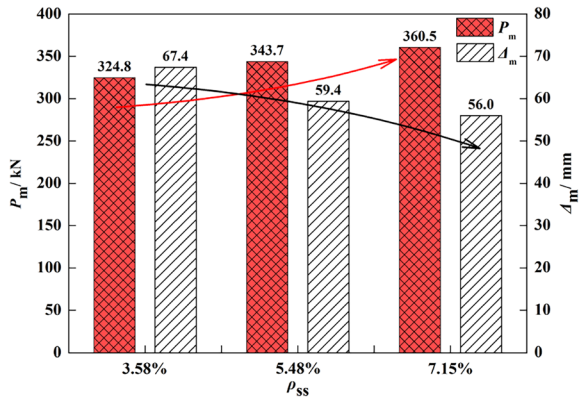

Fig. 23 Influence of peak load and corresponding deflection of SRUHSC frame during the different structural steel ratios

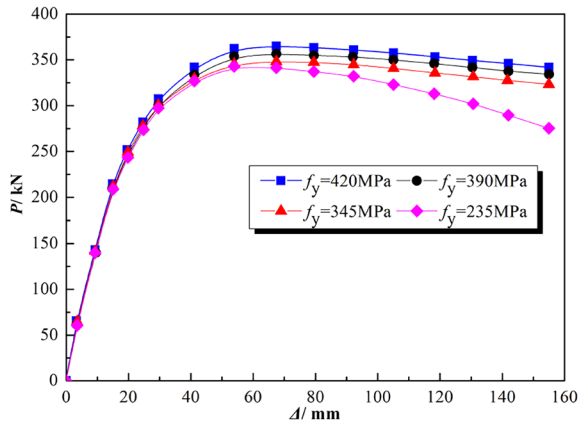

Fig. 24 The relationship of *P-Δ* of SRUHSC frame during the different steel yield strengths in the column

successively selected as steel bones, and the corresponding yield strength f_y is 235 MPa, 345 MPa, 390 MPa and 420 MPa, respectively. The *P-Δ* skeleton curves of finite element simulation are shown in Fig. 24. At the same time, Table 8 shows the influence of the variation of steel bone yield strength on the bearing capacity and deformation capacity of the structure at each loading stage. The meanings of symbols in Table 8 are the same as those in Table 4.

As shown in Fig. 24 and Table 8:

(1) The change of the yield strength f_y has little effect on the stiffness of the structure at the elastic stage, and the *P-Δ* curves almost coincide at this stage.
(2) By increasing the yield strength f_y of steel bones, the peak load of the frame structure and the bearing capacity of the subsequent negative stiffness stage are improved, but the improvement is not obvious and the amplitude is small, Compared with the steel bone whose yield strength f_y is 235 MPa, the ultimate load of Q345, Q390 and Q420 grade steel is increased by 1.05%, 3.55% and 6.05% respectively, and the horizontal displacement Δ_m of the top beam end corresponding to the peak load P_m has little change. The influence of steel bones with different yield strengths on the peak load and corresponding displacement of the frame structure is shown in Fig. 25.
(3) When the yield strength f_y of steel bone in the frame model column increases from 235 to 420 MPa, compared with the peak load P_m, the load P_e of the structure at the end of loading point decreases by 19.9%, 7.26%, 6.38% and 6.36%, respectively. The results show that the bearing capacity of *P-Δ* curves

Table 8 Influence of steel yield strength on load bearing capacity and deformation under different load conditions

f_y/MPa	P_q/kN	P_m/kN	P_e/kN	Δ_q/mm	Δ_m/mm	Δ_e/mm
235	274.3	343.7	275.1	24.8	59.4	155.0
345	276.1	347.3	322.1	24.8	64.7	155.0
390	278.2	355.9	333.2	24.8	67.4	155.0
420	280.3	364.5	341.3	24.8	67.4	155.0

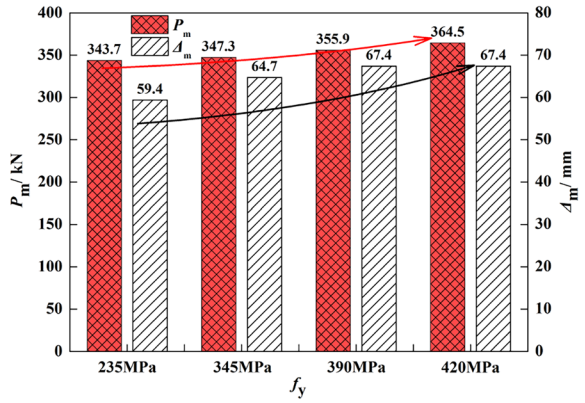

Fig. 25 Influence of peak load and corresponding deflection of SRUHSC frame during the different steel yield strengths in the columns

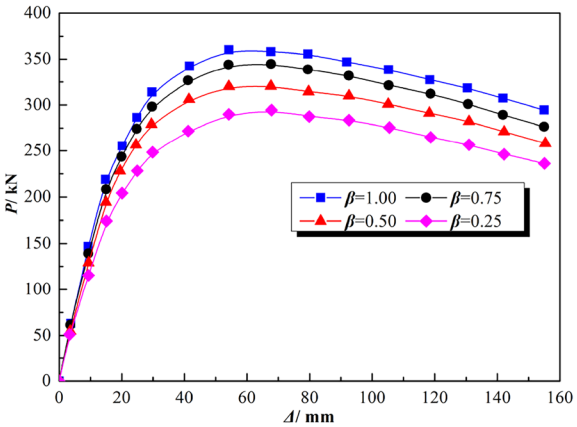

Fig. 26 The relationship of *P-Δ* of SRUHSC frame during the different beam-column's linear stiffness ratios

decreases to some extent at the negative stiffness stage, and the larger the yield strength of steel bones, the smaller the decline, the slower the curve decline, and the better the ductility of the structure.

5.6 Parameters of the Beam-Column's Linear Stiffness Ratio of Frame *β*

In frame structures, the constraint degree of beam to column is characterized by the beam-column's linear stiffness ratio β. The different beam-column's linear stiffness ratio β indicates the different constraints of beams on columns. This difference will make the frame columns have different lateral displacement and angular capacity, which will affect the calculated length, and finally lead to the change of the overall bearing capacity of the frame structure. Therefore, the beam-column's linear stiffness ratio is an important parameter that affects the seismic performance of frame structures. Keeping other parameters unchanged, this paper only adjusts the difference of beam-column's linear stiffness ratio β by changing the span l_n of the frame model beam, so as to study its influence on the mechanical properties of SRUHSC frame structure. For the frame structure, the beam-column's linear stiffness ratio β of the side column or the middle column position should be calculated according to the general layer and the bottom layer respectively. Here, the beam-column's linear stiffness ratio β takes the middle column position of the bottom layer of the frame, and its value is 0.25, 0.50, 0.75 and 1.00, respectively. The *P-Δ* skeleton curves of finite element simulation are shown in Fig. 26. Meanwhile, Table 9 shows the influence of the change of beam-column's linear stiffness ratio on the bearing capacity and deformation capacity of the frame structure at each loading stage. The meanings of symbols in Table 9 are the same as those in Table 4.

As shown in Fig. 26 and Table 9:

(1) The change of beam-column's linear stiffness ratio has a certain impact on the initial elastic stiffness of the frame structure and the peak of the horizontal load. When β is 0.25, the horizontal load of the model structure when the first beam end plastic hinge is generated is 259.5 kN. When the load reaches the peak, it is increased to 292.5 kN until the end of loading. The load at the end point was 235.9 kN, down 19.4% from the peak load.

(2) With the increase of β, the constraining effect of frame beam on frame column is strengthened, and the stiffness and peak load of the model structure at the elastic stage are increased. Compared with the peak load when β was 0.25, the peak load when β was 0.50, 0.75 and 1.00 increased by 9.64%, 18.2% and 23.4%, respectively, indicating that the whole bearing capacity of the beam was effectively improved under the restriction of the column. The influence of different beam-column's linear stiffness ratios on the peak load and corresponding horizontal displacement of the whole structure is shown in Fig. 27.

(3) The horizontal displacement Δ_m of the top beam end corresponding to the peak load P_m with different beam-column's linear stiffness ratio β decreased but was close. In addition, β increased from 0.25 to 1.00, the load P_e at the end of loading point decreased by 19.4%, 19.5%, 19.8% and 17.6%, respectively, compared with the peak load P_m, and the decline trend of negative stiffness of skeleton curve was consistent, indicating that different β had little effect on the displacement ductility of frame structures.

Table 9 Influence of beam-column's linear stiffness ratios of frame on load bearing capacity and deformation under different load conditions

β	P_q/kN	P_m/kN	P_e /kN	Δ_q/mm	Δ_m/mm	Δ_e/mm
0.25	259.5	292.5	235.9	34.5	63.2	155.0
0.50	271.7	320.7	258.3	28.3	61.7	155.0
0.75	276.3	345.7	277.1	25.8	59.4	155.0
1.00	278.2	360.8	297.3	21.7	55.7	155.0

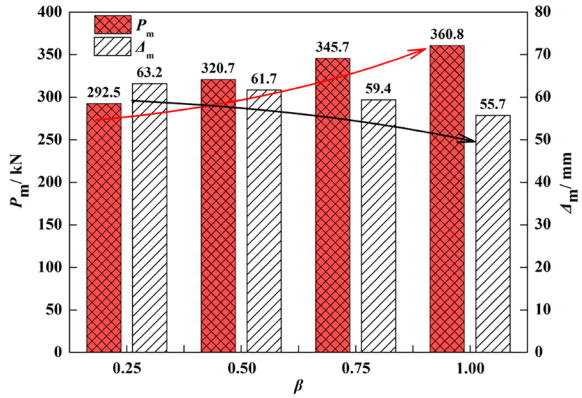

Fig. 27 Influence of peak load and corresponding deflection of SRUHSC frame during the different beam-column's linear stiffness ratios

6 Conclusions

Based on the experimental study on the seismic performance of SRUHSC frame structure system under low cyclic load, nonlinear finite element analysis was carried out with ABAQUS, and the experimental values were compared with the calculated values. The main conclusions were drawn as follows:

(1) In this paper, pseudo-static tests are carried out on the SRUHSC frame, and the main seismic index data such as displacement ductility, interlayer displacement Angle and energy dissipation capacity of the structure are obtained, indicating that the SRUHSC frame has good collapse resistance and plastic deformation ability, and excellent seismic performance.
(2) The three-dimensional finite element model of SRUHSC frame is established. By selecting appropriate material constitutive relation, reasonably applying load, boundary constraint and cross section contact, the whole process of nonlinear finite element analysis is carried out. The calculated results are in good agreement with the measured results, which verifies the correctness of the established model and lays a foundation for extensive parameter analysis.
(3) To further study the seismic performance of SRUHSC frame, ABAQUS was used to analyze the influence parameters of its *P-Δ* skeleton curve. The results show that with the increase of concrete strength, steel bone yield strength and beam-column's linear stiffness ratio, the horizontal bearing capacity and initial elastic stage stiffness of the structure can be effectively improved, but the ductility of the structure is not improved. The horizontal bearing capacity and displacement ductility of the frame column are significantly improved by increasing the volume hoop ratio and steel content, but the horizontal bearing capacity and displacement ductility of the structure are significantly decreased by increasing the axial compression ratio, except for slightly improving the stiffness of the elastic stage of the structure.

Acknowledgements
Not applicable.

Author contributions
ZHANG J-C: wrote the article, supervised the student, prepared the research plan, carried out the experimental work, shared in the theoretical work, and participated in writing and reviewing the article. JIANG X-G: wrote the article, carried out the experimental work, shared in the theoretical work and shared in the final revision. JIA Z-K: carried out the experimental work, and revised the final revision. CAO M-S: supervised the student, and revised the final revision. JIA J-Q: supervised the student, and revised the final revision. All authors read and approved the final manuscript.

Funding
Open access funding provided by the National Science Foundation for Postdoctoral Scientists of China (Grant No. 2019M661710), the Natural Science Foundation of Jiangsu Province, China (Grant No. BK20211101), the Social Development Science and Technology Innovation Project of Suzhou City, Jiangsu Province, China (Grant No. SS202126). The authors gratefully acknowledge the financial supports.

Availability of data and materials
All data generated or analyzed during this study are included in this published article.

Declarations

Competing interests
The authors declare that they have no competing interests.

Received: 5 January 2024 Accepted: 27 March 2024
Published online: 16 July 2024

References

Aboukifa, M., & Moustafa, M. A. (2021). Experimental seismic behavior of ultra-high performance concrete columns with high strength steel reinforcement. *Engineering Structures, 232*, 111885. https://doi.org/10.1016/j.engstruct.2021.111885

Barbero, E. J. (2023). Finite element analysis of composite materials using Abaqus®. CRC press.https://doi.org/10.1201/9781003108153

Chellapandian, M., Prakash, S. S., & Rajagopal, A. (2018). Analytical and finite element studies on hybrid FRP strengthened RC column elements under axial and eccentric compression. *Composite Structures, 184*, 234–248. https://doi.org/10.1016/j.compstruct.2017.09.109

He, S., Deng, Z., & Yao, J. (2020). Seismic behavior of ultra-high performance concrete long columns reinforced with high-strength steel. *Journal of Building Engineering, 32*, 101740. https://doi.org/10.1016/j.jobe.2020.101740

Hung, C. C., Hu, F. Y., & Yen, C. H. (2018). Behavior of slender UHPC columns under eccentric loading. *Engineering Structures, 174*, 701–711. https://doi.org/10.1016/j.engstruct.2018.07.088

Hung, C. C., & Yen, C. H. (2021). Compressive behavior and strength model of reinforced UHPC short columns. *Journal of Building Engineering, 35*, 102103. https://doi.org/10.1016/j.jobe.2020.102103

Kim, S., Shin, J., & Kim, W. (2024). Assessing the seismic performance of exterior precast concrete joints with ultra-high-performance fiber-reinforced concrete. *International Journal of Concrete Structures and Materials, 18*(1), 1–16. https://doi.org/10.1186/s40069-023-00646-9

Krahl, P. A., Gidrão, G. D. M. S., & Carrazedo, R. (2018). Compressive behavior of UHPFRC under quasi-static and seismic strain rates considering the effect of fiber content. *Construction and Building Materials, 188*, 633–644. https://doi.org/10.1016/j.conbuildmat.2018.08.121

Liu, W., & Jia, J. (2018). Experimental study on the seismic behavior of steel-reinforced ultra-high-strength concrete frame joints with cyclic loads. *Advances in Structural Engineering, 21*(2), 270–286. https://doi.org/10.1177/1369433217717116

Ma, G., Hou, C., Hwang, H. J., Chen, L., & Zhang, Z. (2024). Seismic behavior of repairable columns with UHPC segments and replaceable buckling-restrained energy dissipaters. *Engineering Structures, 300*, 117176. https://doi.org/10.1016/j.engstruct.2023.117176

Ma, Y., Jia, J., & Zhu, W. (2018). Comparative analysis of the seismic behaviour of SRUHSC columns and frames under reverse cyclic loading. *Magazine of Concrete Research, 70*(4), 189–203. https://doi.org/10.1680/jmacr.17.00140

Naeimi, N., & Moustafa, M. A. (2020). Numerical modeling and design sensitivity of structural and seismic behavior of UHPC bridge piers. *Engineering Structures, 219*, 110792. https://doi.org/10.1016/j.engstruct.2020.110792

Shafieifar, M., Farzad, M., & Azizinamini, A. (2017). Experimental and numerical study on mechanical properties of ultra high performance concrete (UHPC). *Construction and Building Materials, 156*, 402–411. https://doi.org/10.1016/j.conbuildmat.2017.08.170

Wakjira, T. G., Abushanab, A., & Alam, M. S. (2024). Hybrid machine learning model and predictive equations for compressive stress-strain constitutive modelling of confined ultra-high-performance concrete (UHPC) with normal-strength steel and high-strength steel spirals. *Engineering Structures, 304*, 117633. https://doi.org/10.1016/j.engstruct.2024.117633

Wei, J., Xie, Z., Zhang, W., Luo, X., Yang, Y., & Chen, B. (2021). Experimental study on circular steel tube-confined reinforced UHPC columns under axial loading. *Engineering Structures, 230*, 111599. https://doi.org/10.1016/j.engstruct.2020.111599

Xiaowei, Y. I. N., Xilin, L. U., & Huanjun, J. I. (2013). Analysis of parameters influencing on mechanical behavior of SRC column with high ratio of encased steel. *Journal of Building Structures, 34*(5), 105. https://doi.org/10.14006/j.jzjgxb.2013.05.012

Xu, W., Ma, B., Duan, X., & Li, J. (2021). Experimental investigation of seismic behavior of UHPC connection between precast columns and footings in bridges. *Engineering Structures, 239*, 112344. https://doi.org/10.1016/j.engstruct.2021.112344

Yan, J. B., Chen, A., & Zhu, J. S. (2021). Behaviours of square UHPFRC-filled steel tubular stub columns under eccentric compression. *Thin-Walled Structures, 159*, 107222. https://doi.org/10.1016/j.tws.2020.107222

Yang, Z. C., Han, L. H., & Li, W. (2023). Seismic performance of concrete-encased hexagonal CFST column base: Experimental and numerical analysis. *Journal of Constructional Steel Research, 211*, 108129. https://doi.org/10.1016/j.jcsr.2023.108129

Yao, D., Jia, J., Wu, F., & Yu, F. (2014). Shear performance of prestressed ultra high strength concrete encased steel beams. *Construction and Building Materials, 52*, 194–201. https://doi.org/10.1016/j.conbuildmat.2013.11.006

Zhang, J., & Jia, J. (2016). Experimental study on seismic behavior of composite frame consisting of SRC beams and SRUHSC columns subjected to cyclic loading. *Construction and Building Materials, 125*, 1055–1065. https://doi.org/10.1016/j.conbuildmat.2016.08.157

Zhang, J., Jia, J., Yu, J., & Sun, Z. (2019). Seismic behaviour of steel-reinforced ultra-high-strength concrete composite frame: Experimental study. *Advances in Structural Engineering, 22*(9), 2179–2191. https://doi.org/10.1177/1369433219836180

Zhu, W., Jia, J., Gao, J., & Zhang, F. (2016). Experimental study on steel reinforced high-strength concrete columns under cyclic lateral force and constant axial load. *Engineering Structures, 125*, 191–204. https://doi.org/10.1016/j.engstruct.2016.07.018

Zhu, W. Q., Meng, G., & Jia, J. Q. (2014). Experimental studies on axial load performance of high-strength concrete short columns. *Proceedings of the Institution of Civil Engineers-Structures and Buildings, 167*(9), 509–519. https://doi.org/10.1680/stbu.13.00027

Zhu, Y., Zhang, Y., Hussein, H. H., & Chen, G. (2020). Numerical modeling for damaged reinforced concrete slab strengthened by ultra-high performance concrete (UHPC) layer. *Engineering Structures, 209*, 110031. https://doi.org/10.1016/j.engstruct.2019.110031

Publisher's Note

Jian-cheng Zhang corresponding author, PhD, Associate Professor, Associate Professor of Concrete Structures, School of Naval Architecture and Civil Engineering, Jiangsu University of Science and Technology, Zhangjiagang, Jiangsu 215600, China, and Industrial Technology Research Institute of Zhangjiagang, Jiangsu University of Science and Technology, Suzhou, Jiangsu 215600, China.

Xue-guo Jiang BE, Master's student, School of Civil Engineering and Architecture, Jiangsu University of Science and Technology, Zhenjiang, Jiangsu 212100, China.

Zi-kang Jia BE, Master's student, School of Naval Architecture and Civil Engineering, Jiangsu University of Science and Technology, Zhangjiagang, Jiangsu 215600, China.

Mao-sen Cao PhD, Professor, Associate Professor of Concrete Structures, The College of Mechanics and Materials, Hohai University, Nanjing, Jiangsu 211100, China.

Jin-qing Jia PhD, Professor, Associate Professor of Concrete Structures, The State Key Laboratory of Coastal and Offshore Engineering, Dalian University of Technology, Dalian, Liaoning 116024, China.